JGR Solid Earth

RESEARCH ARTICLE
10.1029/2019JB018697

High-Resolution 3-D *P* Wave Velocity Structures Under NE Taiwan and Their Tectonic Implications

Po-Li Su[1], Po-Fei Chen[1], and Chien-Ying Wang[1]

[1]Department of Earth Sciences, National Central University, Taoyuan City, Taiwan

Key Points:
- High-resolution tomography conducted in northeast Taiwan enables us to investigate its tectonic implications
- The imaged high V_p anomalies of the Philippine Sea Plate comply with the subducting indenter model and favor the breakoff model
- Shallow low V_p anomalies beneath the Ilan Plain extend to those beneath the Okinawa Trough

Supporting Information:
- Supporting Information S1

Correspondence to:
P.-F. Chen,
bob@ncu.edu.tw

Citation:
Su, P.-L., Chen, P.-F., & Wang, C.-Y. (2019). High-resolution 3-D *P* wave velocity structures under NE Taiwan and their tectonic implications. *Journal of Geophysical Research: Solid Earth*, *124*, 11,601–11,614. https://doi.org/10.1029/2019JB018697

Received 12 SEP 2019
Accepted 6 OCT 2019
Accepted article online 22 OCT 2019
Published online 16 NOV 2019

Abstract First *P* wave arrival-time data from local earthquakes recorded by a dense geophone array deployed on the Ilan Plain and by existing permanent stations were combined to invert for high-resolution *P* wave velocity structures under northeast Taiwan. With relatively high resolution, we were able to examine the structures in more detail and to investigate their significance and tectonic implications. We introduce two distinct groups of proposals for mechanisms of subduction polarity flipping in Taiwan, referred to as the "tear model" and "breakoff model." While the predicted Philippine Sea Plate boundaries differ between the two models, those of the breakoff model and the related subducting indenter model are geodynamically similar. The surface junction and the west edge of the imaged high V_p anomalous Philippine Sea Plate comply with those predicted by the subducting indenter model and thus favor the breakoff model over the tear model. While the observed high V_p anomalous region in the mantle wedge can be explained as eclogitization of previously subducted crust, eclogitization of the overriding continental crustal roots cannot be ruled out. Those beneath the Taipei Basin and the Tatun Volcano Group exhibit a pattern potentially connected to the low V_p anomalies in the mantle wedge, suggesting the involvement of the Philippine Sea slab, either by asthenospheric upwelling due to extensional collapse or by fluid migration due to slab dehydration. Those beneath the Ilan Plain exhibit a low V_p pattern extending to deeper origins in the eastern offshore region, suggesting a connection with the opening of the Okinawa Trough.

1. Introduction

Taiwan is located on the convergent boundaries between the Philippine Sea Plate (PSP) and the Eurasian Plate (EUP), where the ~8-cm/year northwestward convergence rate were accommodated by subduction offshore and collisional orogeny on land. The polarity of subduction flips from the east dipping Manila Trench offshore south Taiwan to the north-northwest dipping Ryukyu Trench offshore NE Taiwan. The island of Taiwan itself is formed by orogenic processes resulting from the collision between the NE trending Chinese continental shelf and the northern Luzon Arc (Ho, 1986). Behind the southern segment of the Ryukyu Trench, subduction of the PSP also induced the opening of a back-arc basin, known as the Okinawa Trough, where the latest opening reactivated since 2 Ma ago and proceeded southward (Sibuet et al., 1987). The Ilan Plain in NE Taiwan is located at the southwest end of the Okinawa Trough and may signify onshore rifting of the back-arc basin (Figure 1; Hou et al., 2009).

Flipping of the subduction polarity is geodynamically inevitable when the oceanic lithospheres of two plates collide with each other, and the two primary processes involved in the tectonics of Taiwan demonstrate this. First, consumption of the oceanic lithosphere of one plate by subduction was followed by arc collisions with the approaching continental lithosphere (e.g., present-day south-central Taiwan). Second, as the collisions continued, the oceanic lithosphere of the other plate (e.g., the PSP) needed to be subducted, resulting in a flipping of the subduction polarity. However, it is intriguing to determine how the upper mantle (e.g., that beneath NE Taiwan) accommodates slabs of opposite polarities subducted one after another. Several models have been proposed to understand the 3-D tectonic configurations and flipping mechanisms in Taiwan. In the following, we introduce and distinguish two distinct groups of proposals, hereinafter referred to as the "tear model" and the "breakoff model."

For the "tear model," a lithospheric tear on the EUP is necessary to explain that the same EUP subducts beneath Taiwan and overrides the PSP along the Ryukyu Arc (T1 in Lallemand et al. (2001)). Based on 3-D plate configurations reconstructed from global tomography results (Bijwaard et al., 1998), the tear has first propagated westward along the continent-ocean boundary (near 24°N) to 123°E and then

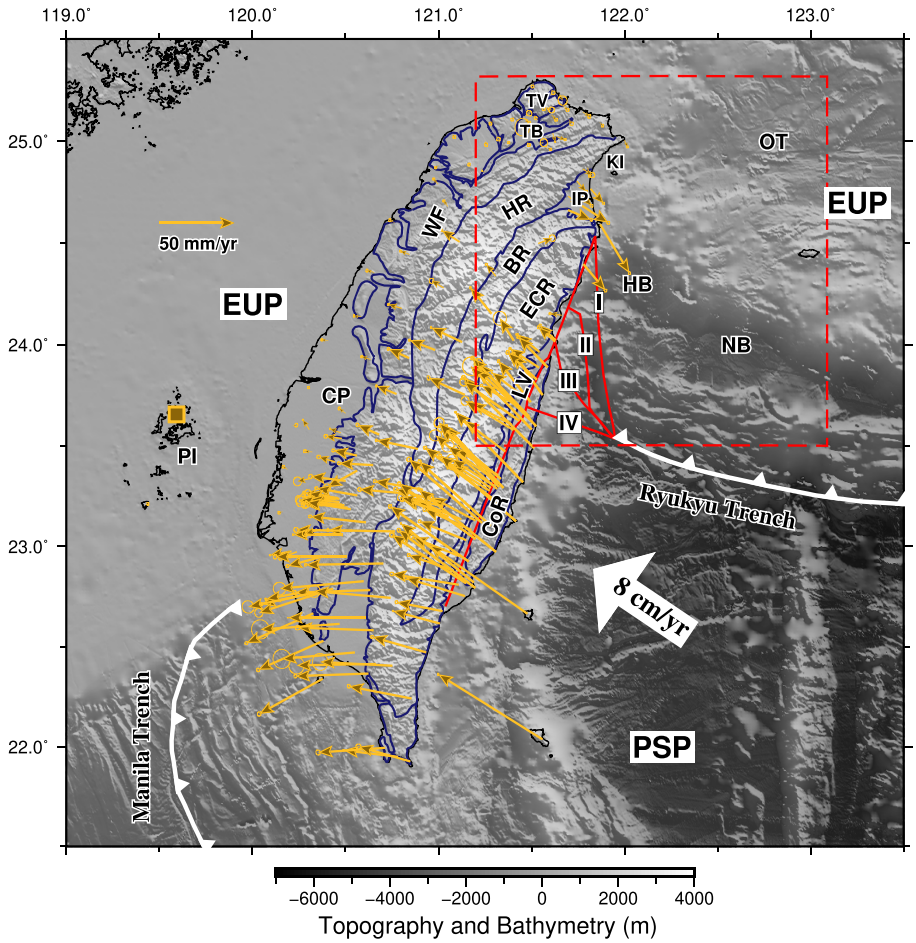

Figure 1. Regional tectonic setting of Taiwan and the GPS velocity field (brown vectors) relative to Paisha, Penghu (brown square), excerpted from Hsu et al. (2009). The four previously proposed models for the EUP-PSP junction are denoted by solid red lines (see text). The white arrow indicates the relative motion of PSP–EUP, and the dashed red lines surround the study region. TV = Tatun Volcano Group, TB = Taipei Basin, OT = Okinawa Trough, KI = Kueishantao Island, IP = Ilan Plain, HR = Hsuishan Range, WF = West Foothill, BR = Backbone Range, ECR = East Central Range, HB = Hoping Basin, NB = Nanao Basin, LV = Longitudinal Valley, CP = Coastal Plain, and CoR = Coastal Range.

northwestward through the continental lithosphere to 121.5°E. The northwest propagation rates of the tear should be the same as the EUP-PSP convergence rates, in order for the westerly migration of the PSP slab, resulting in flipping of subduction polarities. The NW-SE tearing through continental lithosphere between 121.5°E and 123°E was attested by patterns of seismicity distributions (Engdahl et al., 1998) and free-air gravity anomalies (Hsu et al., 1998). As a result, the current arc-continent collision in central Taiwan was attributed to subduction of the EUP continental lithosphere with a potential detachment at depth for westerly migration of the PSP slab.

For the breakoff model, not only the initiation of arc-continent collision but also the termination of collision by flipping subduction polarity is progressively propagating southwestward in Taiwan. While the former, currently at South Taiwan, was constructed by a closed velocity triangle using trends of the EUP continental margin, the Luzon Arc, and the EUP-PSP relative motions, the latter, currently at N Taiwan, uses the shape of inactive and active mountain fronts, as well as the EUP-PSP relative motions, assuming a steady-state mountain width. As a result, Suppe (1984) concluded that the collision, flipping, and back-arc spreading have been propagating along the continental margin at the same rate since the Pliocene. To accommodate both slabs of flipping subduction polarity, Teng et al. (2000) proposed a breakoff of the east dipping EUP slab beneath N Taiwan where the collision has terminated.

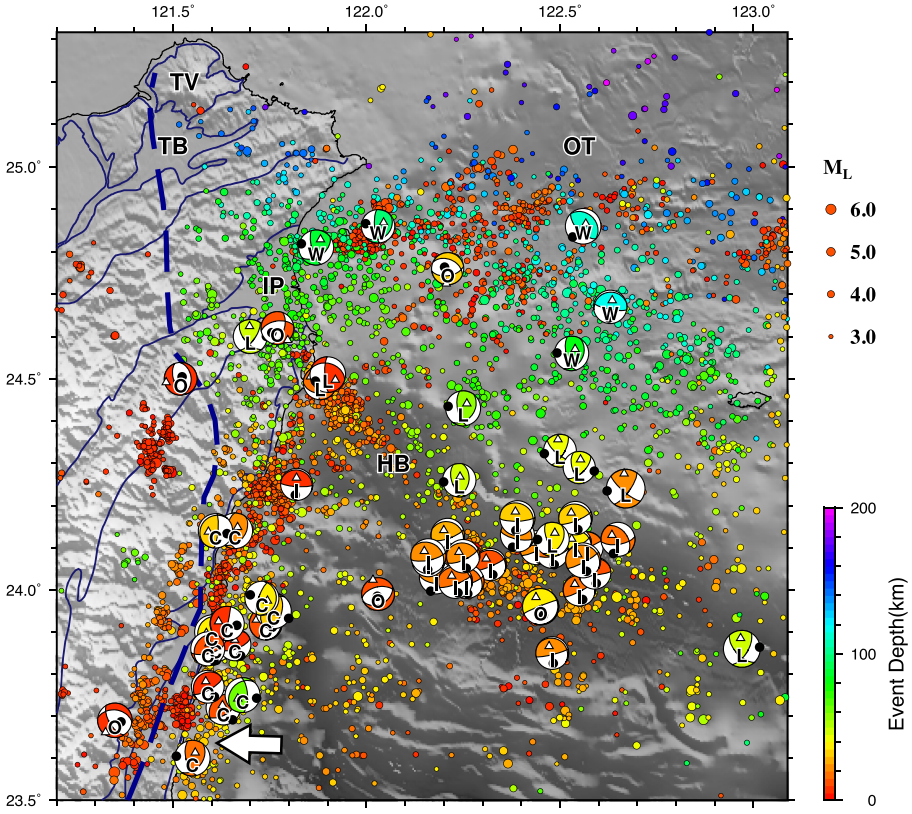

Figure 2. Seismic distributions and spatial characteristics of focal mechanisms within the NE Taiwan study area. Only Central Weather Bureau (CWB) catalog events with M_L greater than 3 and depths less than 200 km are shown for the seismicity, and the focal mechanism results from Kao et al. (1998) are adopted and marked with C, I, L, W, and O for CSZ, ISZ, LCSZ, WBSZ, and OSZ (see text), respectively. The ***P*** and ***T*** axes of the focal mechanisms are denoted by the black circles and triangles, respectively. The dashed blue line indicates the surface projection of the west boundary of PSP as proposed by Wu et al. (2009).

The tear and breakoff models, respectively, are associated with certain geophysical observations, such as (a) the EUP-PSP junction in East Taiwan, (b) the west edge of PSP (WEP) beneath North Taiwan, (c) patterns of earthquake distributions and focal mechanisms, and (d) surface deformations that can be used as a verdict. For (a), because the bathymetric low of the Ryukyu Trench west of 121.95°E was blurred by collisional deformation, Wu et al. (2009) pointed out that there are four models in the literature to depict how the Ryukyu Trench connects to Taiwan westward, that is, location of the EUP-PSP junction (Figure 1; Angelier et al., 1990; Font et al., 2001; Lallemand et al., 1997; Wu et al., 1997). Among them, model II (and the like) is mostly favored by the tear model, corresponding to its NW propagation, which results the location of North Luzon Arc offshore NE Taiwan between the collision boundary to the west and the subduction boundary to the east (Font et al., 2001; Lallemand et al., 2001). Model IV, based on local catalog seismicity (Wu et al., 1997), extends the Ryukyu Trench W of 121.95°E westerly to the east coast of Taiwan at 23.7°N, south of Hualien. Geodynamically speaking, model IV is mostly compatible with the breakoff model because the detached EUP slab opened a mantle window for NW or west movements of PSP slab. Likewise for (b), WEP tends to migrate more westerly beneath North Taiwan for the breakoff model. According to Teng et al. (2000), WEP could reach as far westward as 121°E beneath North Taiwan.

For (c), Kao et al. (1998) compiled patterns of earthquake ($5.5 \leq m_b \leq 6.6$) focal mechanisms in NE Taiwan and offshore and distinguished five major seismogenic structures (Figure 2)—Collision Seismic Zone (CSZ), Interface Seismic Zone (ISZ), Lateral Compression Seismic Zone (LCSZ), Wadati-Benioff Seismic Zone (WBSZ), and Okinawa Seismic Zone (OSZ). CSZ events are those in the east coast south of 24.3°N with *P* axes subparallel to the PSP–EUP convergence direction. ISZ events ($10 \leq d \leq 35$ km) are those near the SE edge of Hoping Basin with a nodal plane of low-angle thrust dipping to N or NNW. LCSZ events

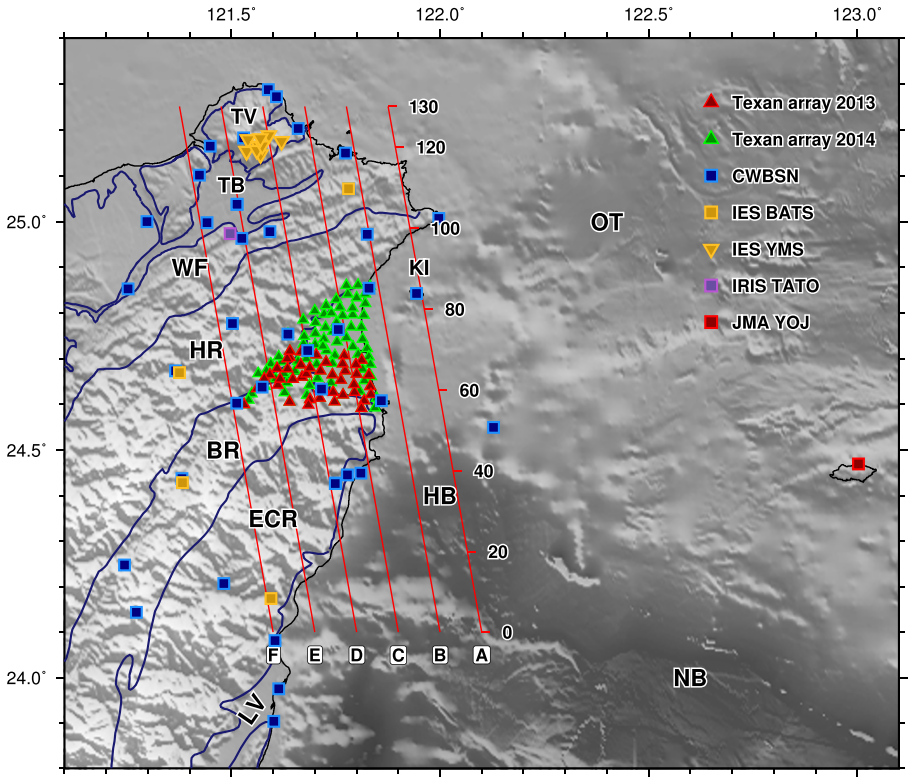

Figure 3. Distributions of the stations used for tomographic studies with different symbols and colors to mark the different network groups. Note the dense Texan array on the Ilan Plain (the red and green triangles), which was deployed for this study. The red lines denote the locations of six cross-section profiles westward from A to F (shown in Figure 6) with distances in kilometers noted relative to the southernmost point of the profile shown in profile A.

($40 \leq d \leq 60$ km) are those easterly along the southern edge of the Ryukyu Arc with *P* axes in E/W direction. WBSZ refers to deeper events associated with PSP subducting slab, and OSZ refers to shallow events associated with Okinawa Trough. Based on the observations that ISZ events gradually bend northward with increasing dip angle as it approaches Taiwan, Kao et al. (1998) suggested that the EUP-PSP junction follows that of model II. However, more recent hypocentral distributions using double-difference relocation revealed that the shallow seismicity belt between the NE coast of Taiwan and 123°E indeed appears to be two WNW trending segments offset by about 30 km in the middle. Both zones exhibit nearly vertical seismicity on top of a dipping seismic zone (40–50 km) and thus cannot be used as an indication for the EUP-PSP boundary (Wu et al., 2009).

Together with seismicity and 3-D velocity structures, Wu et al. (2009) proposed a subducting indenter model that the EUP-PSP junction follows Model IV to intersect East Taiwan at 23.7°N. South of 23.7°N, the EUP and PSP are in direct impact by the collision, whereas north of 23.7°N, the WEP began submerging toward the north and then turned NW below about 60 km to move under the Tatun Volcano Group (Figure 2). Two features of seismicity support this model. The first one is the bottom of the Wadati-Benioff zone along the Longitudinal Valley and the Coastal Range exhibiting bending initiated at 23.7°N (bottom bending) and corresponding to CSZ (white arrow in Figure 2). The second one is the WBSZ west of 123°E remaining in an E-W trend, not turning NW. For (d), GPS observations on the NW movement of the Coastal Range relative to stable EUP continent exhibit a decrease from south to north (Hsu et al., 2009). That the initial point of rapid decrease coincides with that of the proposed junction is consistent with initial submergence of WEP toward north (Figure 1).

During the period between 2013 and 2015, we deployed a high-density Texan array (~5-km station interval) on the Ilan Plain (Figure 3). While the main purpose of this deployment is to derive high-resolution velocity structures for geothermal exploration (Chen et al., 2016), incorporating data from existing permanent

stations in the vicinity enables us to broaden the array aperture to investigate those beneath NE Taiwan, as justified by checkerboard tests. In this study, we firstly conduct a tomography study to invert high-resolution *P* wave structures beneath NE Taiwan. The results are compared with those of previous tomography studies and then presented in the framework of Taiwan tectonics. Finally, we attempt using the results to discriminate between the tear model and breakoff model and, in turn, using the latter to explain our results.

2. Data and Data Processing

The dense Texan array on the Ilan Plain was deployed with data acquisition in two phases. The first phase spanned from June to November of 2013 with 43 stations that covered the southern Ilan Plain (Chen et al., 2016), and the second phase spanned from August 2014 to January 2015 with 108 stations that covered extensively the entire Ilan Plain (Figure 3). The instrument used was a Geospace GS-11D vertical geophone with a peak response at 4.5 Hz connected to a Texan digitizer (REF TEK RT-125A) with a 100-Hz sampling rate. We employed the Antelope software package (http://www.brtt.com) for most of the data storage and processing, including automatic picking of first arrivals and locating of the associated events (preliminary hypocenters). The former was done by short-term average over the long-term average (Allen, 1982) and the latter by a grid search over a volume bounded by 121.15°E–122.35°E, 24.11°N–25.31°N, and 0–100 km in depth. We discarded picks without associated events and refined the remaining picks using the Akaike information criterion algorithm (Zhang et al., 2003). The final picks were visually confirmed with assigned uncertainties and were used for relocations by a 1-D velocity model of NE Taiwan (Chen, 1995). We discarded again those picks for which there were less than 10 associated with the same event. As a result, a total of 1,665 events with 42,273 first *P* wave arrival measurements were collected.

In order to broaden the array aperture and to extend ray coverages, data of the first *P* arrivals from neighborhood permanent stations were incorporated. For CWB events ($M_L \geq 2$) in the period between January 2010 and March 2015, we kept those events either among the 1,665 events (1,587 events) or that have at least 14 good quality level (QL $\leq$ 2 in the CWB catalogue) readings (Shin et al., 2013). Only QL $\leq$ 3 picks of kept events were used. There is an additional criterion for events east of 122.08°E that readings of the YOJ station (the easternmost station on Yonaguni Island from the Japan Meteorological Agency Seismic Network) must have QL $\leq$ 2. In the end, a total of 6,060 events with 184,367 first arrivals were retained for the velocity inversion. According to the final station-event distributions, the target region of tomography was bounded by 121.29–122.9°E, 23.95–25.24°N, and 0–150 km in depth (Figure 4).

3. Methods

The region for tomographic study was parameterized into 3-D velocity grids with grid spacings of 2, 4, and 10 km as adjusted by reduction of ray densities when moving away from the Ilan Plain (Figure 4). Using the grids and an initial 1-D velocity model for NE Taiwan (Figure S2a; Chen, 1995), we applied the FDtomo package (Roecker et al., 2006) for inversions of the optimal 3-D velocity structures and hypocentral locations that best fit data of first *P* arrivals. The optimum values of damping and smoothing factors were determined separately by examining the trade-off curves of each with respect to data misfit. In general, a stable solution was reached after 15 iterations. We conducted both checkerboard and spike tests to evaluate the reliability of the overall results and whether the observed anomalies are genuine. Finally, we performed the inversions with and without data of the dense Texan array and concluded that the former mainly improves the resolution of shallow structures, especially those beneath the Ilan Plain. More detailed descriptions of methods can be found in the supporting information. After 15 iterations, we reached the final 3-D *P* wave velocity model with which the data variance was reduced by 48%, from 0.0180 to 0.0087 s^2. The residual distributions of the initial 1-D and final 3-D velocity structures are shown in Figure S2a.

4. Results

We present the results in three fashions: they are, in order, depth slices, vertical profiles, and 3-D visualizations. In these figures, −1% and +1% V_p horizontal perturbations are indicated in 2-D images by red and blue lines, respectively, and are used to illustrate outlines of high and low V_p anomalies in 3-D perspective views, respectively. Figure 5 shows the horizontal perturbation of the final *P* wave velocity model for six depth slices. In the shallow region (e.g., at a depth of 4 km), the V_p anomalies generally correspond to the

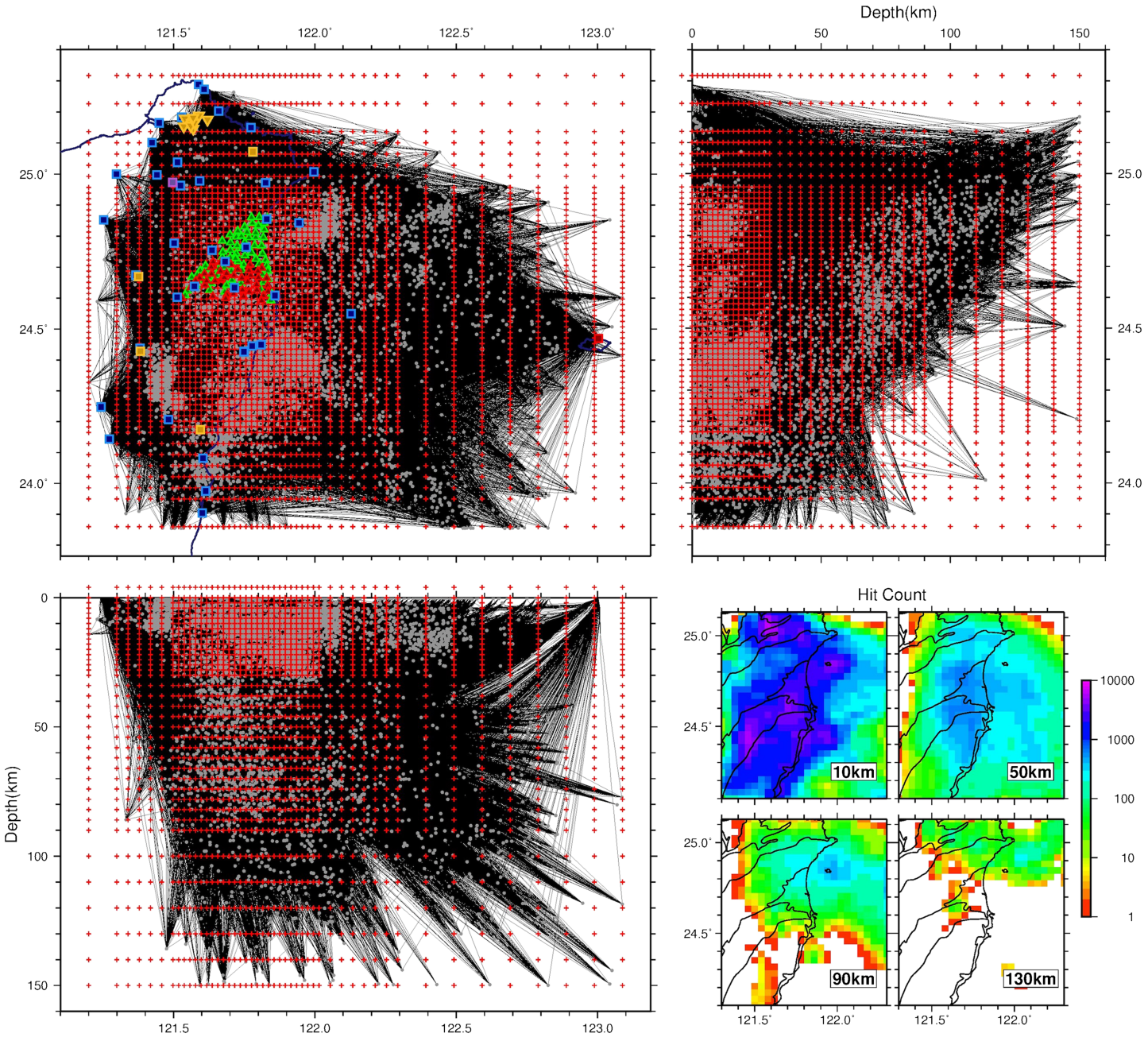

Figure 4. Ray coverage and distribution of the velocity grid points (the red crosses) in the study area for the 3-D *P* velocity inversion shown in (top left) map view, the (top right) north-south (N-S) cross section, and the (bottom left) E-W cross section. The hit counts of the rays at various depths are shown in the bottom right panel.

known geologic units, for example, the high V_p anomalies beneath the NE-SW trending mountain ranges and the low V_p anomalies beneath the Taipei Basin and the Ilan Plain. The low V_p anomaly beneath the Taipei Basin (L2) exhibits high intensity and persists to depths below 10 km, while the one beneath the Ilan Plain (L1) is only seen in shallow regions. However, the low V_p anomaly beneath the Ilan Plain (L1) appears to be connected to an E-W trending low V_p anomaly in the Okinawa Trough at a depth of 10 km, which will be easier to identify later in 3-D perspective views. At a depth of 20 km, the high V_p anomalies beneath the Central Range at shallow depths are replaced by low V_p anomalies. This change in the sign of the V_p anomaly is consistent with previous observations (e.g., Huang et al., 2014; Kuo-Chen et al., 2012),

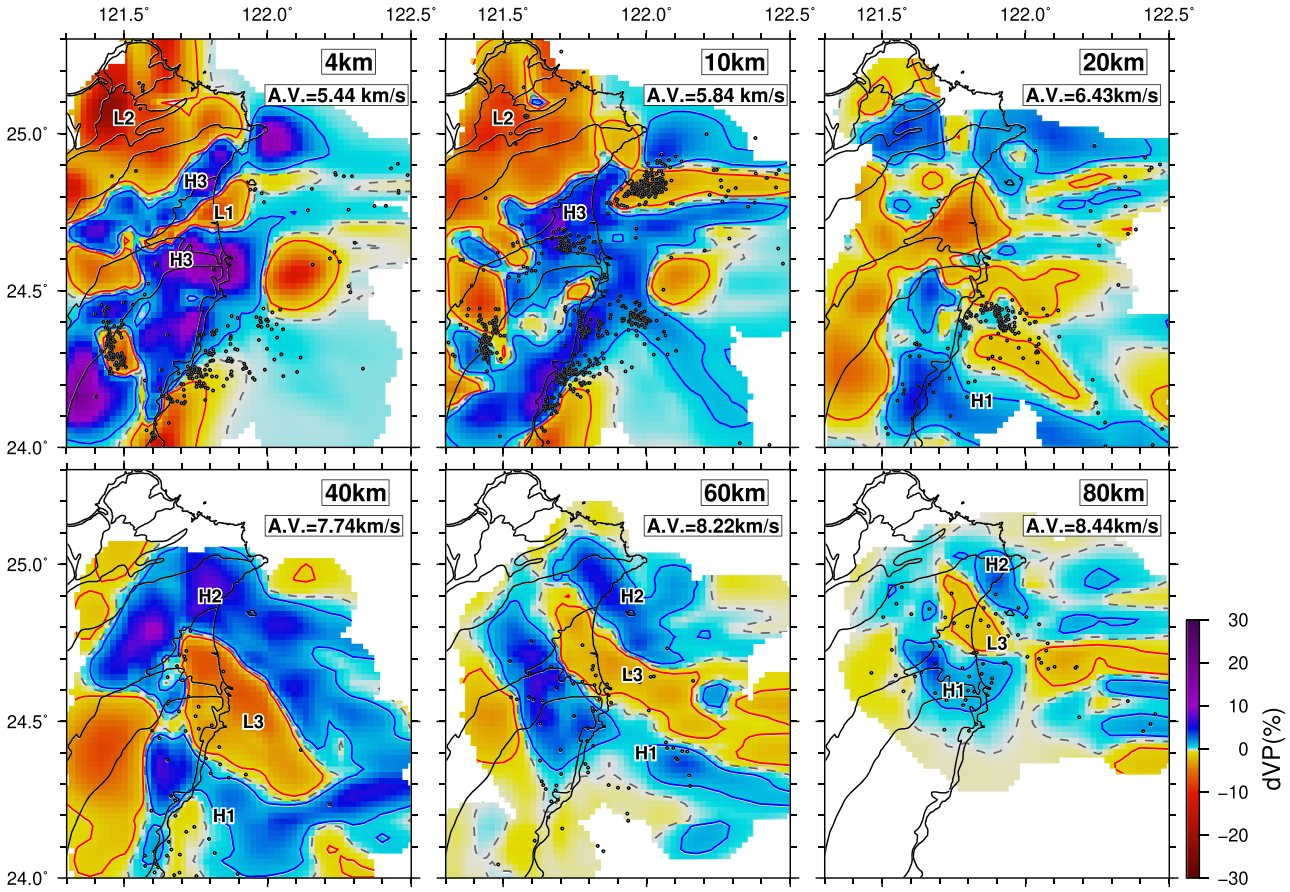

Figure 5. Depth slices of the fractional perturbations in the *P* wave velocity relative to the average velocity at the depth shown in the top right hand corner of each panel. Red, dashed, and blue lines represent −1, 0, and +1% V_p perturbations, respectively. Dots indicate the distributions of the earthquakes.

and these low anomalies have commonly been interpreted as the thickened crustal root induced by the collision. Another notable feature at a depth of 20 km is a high V_p anomaly (H1) which is perpendicular to the trend of the mountain ranges and extends from the eastern offshore region to the Central Range. This high V_p anomaly gradually moves northward with increasing depth (see the 40-, 60-, and 80-km depth slices). Together with this high V_p anomaly, a low V_p anomaly (L3) above and a high V_p anomaly (H2) tens of kilometers to the north dominate the velocity image from depths of 20 to 80 km.

Figure 6 shows the absolute *P* wave velocities and the fractions of the horizontal perturbations along six profiles (A–F in Figure 3), from east to west running approximately in the N-S direction and covering NE Taiwan and the eastern offshore region. Generally speaking, the resulting patterns can be divided into shallow (<20 km) and deep (>20 km) patterns. For the shallow patterns, a good correspondence for the low V_p anomalies beneath the basins (e.g., the Taipei (L2) and Ilan (L1) basins) and the high V_p anomalies beneath the mountain ranges (e.g., the Hsuishan and Backbone ranges (H3)) was observed. For the deep patterns, features that were persistently observed in all of the profiles (except F) include a north dipping high V_p anomaly representing the subducted PSP slab (H1), a low V_p anomalous zone above the PSP slab (L3), and a volume of high V_p anomalies in the mantle wedge tens of kilometers from the PSP slab (H2). The extent and feature of each anomaly can be visualized in 3-D perspective views (Figures 7–9). The patterns are in general consistent with previous studies (e.g., Huang et al., 2014; Kuo-Chen et al., 2012). Furthermore, the Moho variations as traced by the isovelocity contour of V_p = 7.5 km/s also agree with previous observations that the deepest point is located at a depth of approximately 40–45 km beneath the Backbone Range and the Ilan Plain.

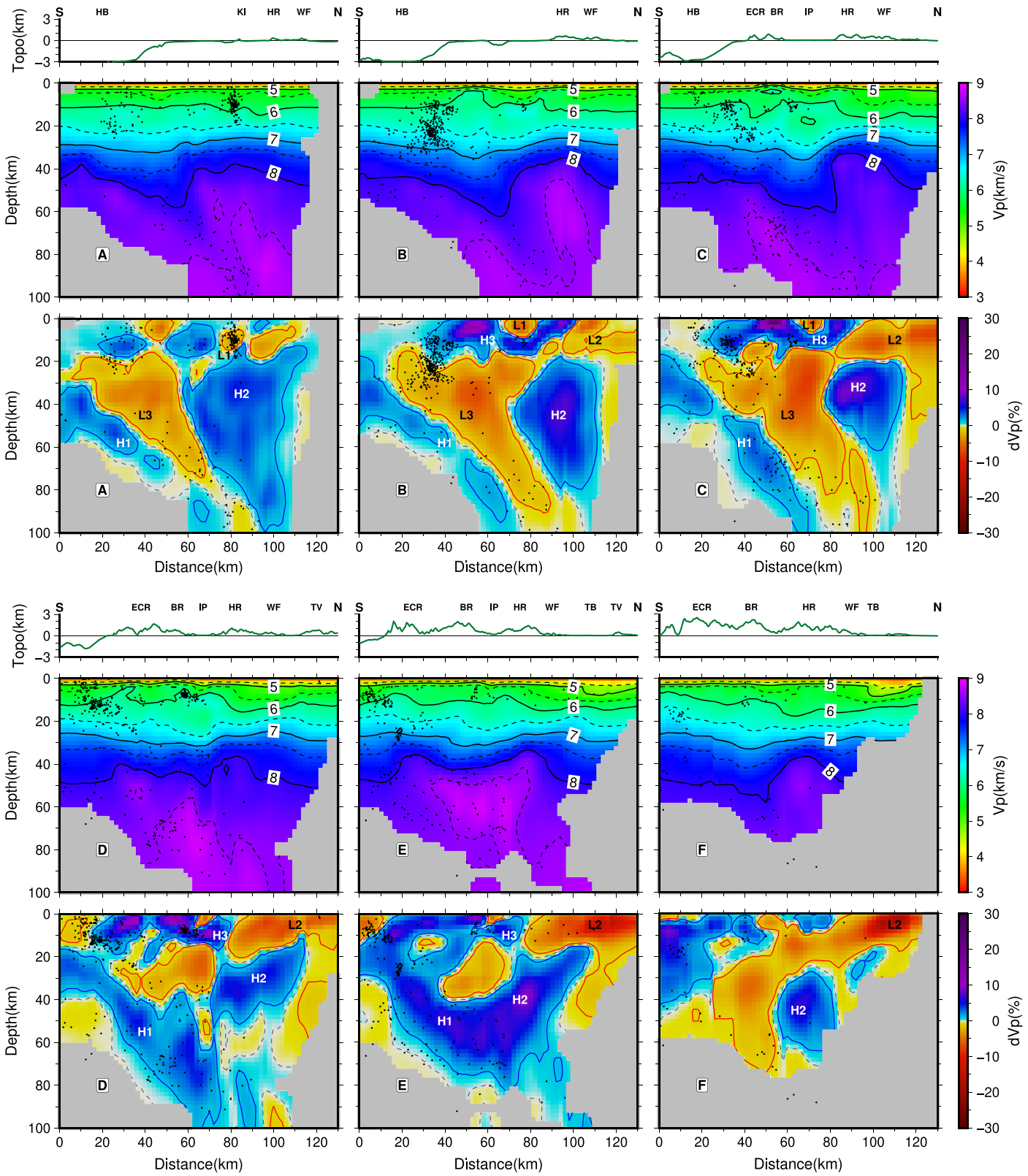

Figure 6. (the first and third rows) Absolute value and (the second and fourth rows) fractional horizontal perturbations in the *P* wave velocity for the six profiles, A–F. Dots indicate the distributions of the earthquakes. Contours in the absolute velocity image are isovelocity at 0.5-km/s intervals. Red, dashed, and blue lines in the perturbation images represent −1, 0, and +1% V_p perturbations, respectively. The topography along each profile is shown on top of the absolute velocity image with the same abbreviations as those used in Figure 1.

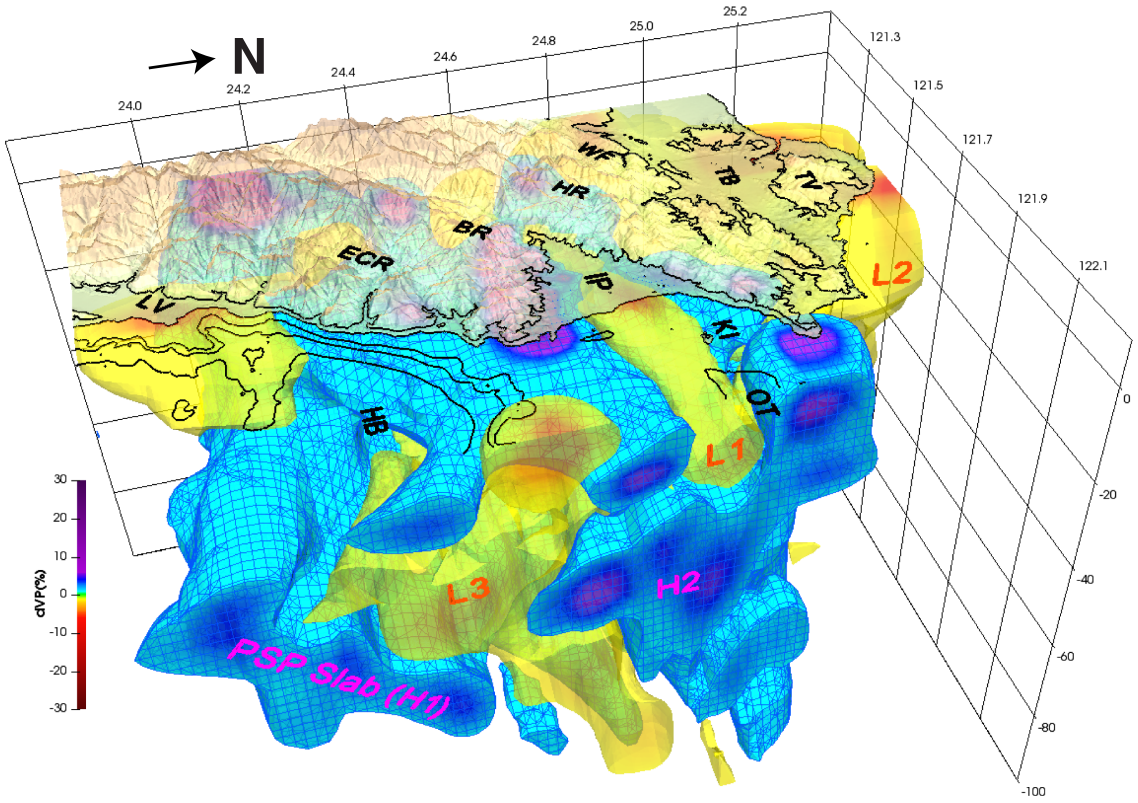

Figure 7. A 3-D visualization of the imaged crustal and upper mantle velocity structures in the southern termination of the Ryukyu subduction against NE Taiwan. Low and high V_p structures are bounded by the −1% and +1% isosurfaces, respectively, of the *P* wave velocity perturbation (dV_p). The topography (the transparent surface above the velocity structures) and bathymetry (solid contours) are superimposed for comparison. The eastern boundary of the figure is clipped at 122.1°E.

Next, we inspect the westward variations in the shallow patterns from profiles A–F, followed by an inspection of the deep patterns. In profile A, beneath an offshore volcanic island (Kueishantao Island), there are low V_p anomalies at a depth of approximately 10 km with average radius of ~6 km for the −1% isosurface (L1) together with clustered seismicity distributions, suggesting the presence of magmatic activity. In profile B, the two zones of low V_p at depths of less than 10 km indicate a correspondence of the low V_p anomalies with the Taipei (L2 at a distance of 110 km) and Ilan (L1 at a distance of 75 km) basins. The anomalies beneath the Ilan Plain are intercepted by a layer of high V_p anomalies (H3) which correspond well to the mountain ranges on the surface. Note that the seismicity cluster beneath the north edge of the Hoping Basin (at a distance of 30 km) is distributed in a nearly vertical trend down to a depth of 40 km across the border of low and high V_p anomalous zones. The correspondence observed in profile B is more distinctive in profile C, which cuts right through the Ilan Plain. The patterns beneath the Western Foothills near the Tatun Volcano Group (L2) exhibit a large number of low V_p anomalies and a potential connection with the low V_p anomalous region in the mantle wedge (L3). In profile D, while the low V_p anomalies decrease beneath the edge of the Ilan Plain, those beneath the edge of the Taipei Basin increase both in strength and lateral extent as the profile approaches the Tatun Volcano Group. The high V_p anomalies still correspond well to the mountain ranges on the surface. The patterns in profile E resemble those in profile D, with a significant number of low V_p anomalies beneath the Taipei Basin and the Tatun Volcano Group. In profile F, a minor low V_p anomaly is observed beneath the boundary between the Hsuishan Range and Backbone Range. This minor anomaly appears to be connected to another low V_p anomaly at depth.

For the deep patterns, in profile A, the high V_p anomaly associated with the subducted PSP slab (H1) is revealed at depths greater than 30 km beneath the Hoping Basin dipping to the north (Figure 6). In profile B, the *P* wave velocity contrasts are more significant, exhibiting the typical features of the PSP slab (H1), a low V_p anomalous zone (L3), and an area of high V_p anomalies (H2). The velocity structure in profile C is

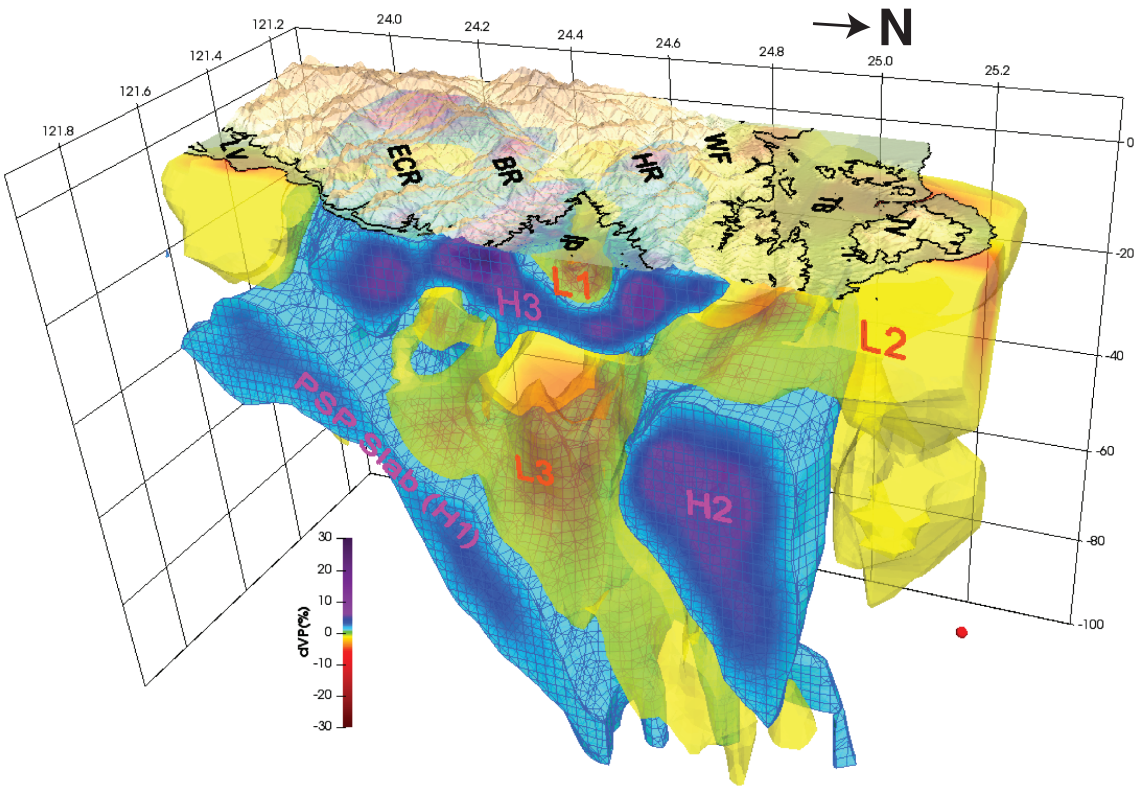

Figure 8. A 3-D visualization of the resulting velocity structures from NE to SW with the eastern boundary clipped at 121.8°E. The red dot beneath Taipei shows the relocated hypocenter (121.52°E, 25.28°N; 75-km depth) of the 1909 M_W 7 deep intraplate earthquake (Kanamori et al., 2012).

similar, with the strength of the low V_p anomalies (L3) reaching its maximum and growing wider at greater depths (>60 km). However, in profile D, the low V_p anomalies in the mantle wedge show a sudden reduction in strength, which results from the close proximity to the PSP slab and the high V_p anomalous area at depths greater than 45 km. In profile E, the contact areas of the PSP slab and the high V_p anomalous area in the mantle wedge are observed below depths of 45 km (Figure 9). In profile F, the high V_p anomaly of the PSP slab is replaced by the low V_p anomaly of the thickened crustal root (Figure 9 and section 5), implying that the western boundary of the PSP is between profiles E and F.

5. Discussion

In comparisons with results of previous studies, we compare the structures in our profiles B and C to those of Profile 2 in Figure 9 of Lin et al. (2004), the cross section along longitude 121.8°E in Figure 3 of Chou et al. (2009), and profiles GG′ and HH′ in Figure 6 of Huang et al. (2014). We find that the high V_p anomalies of the subducted PSP slab (H1) and the conspicuous low V_p anomalies atop the PSP slab (L3) are consistently imaged by all these studies. Next, the presence of an area of high V_p anomalies (H2), which differs from the low V_p anomalies of a typical mantle wedge (e.g., Zhao et al., 2009), was observed by Huang et al. (2014) and Lin et al. (2004). In their results, the area exhibits not only high V_p but also high V_s anomalies. Finally, crustal structures including the high V_p anomaly (H3) beneath the mountain ranges and the low V_p anomalies that reside in the two basins resemble those of Huang et al. (2014). In addition, the observation of low velocities beneath the Central Range (e.g., in the 20-km depth slice in Figure 5) is consistent with those of Kuo-Chen et al. (2012) and Huang et al. (2014). In conclusion, our results are generally robust and are not unprecedented when compared to previous studies. In this study, however, the high-resolution results for specific regions beneath NE Taiwan validate the examinations and interpretations of more detailed structures.

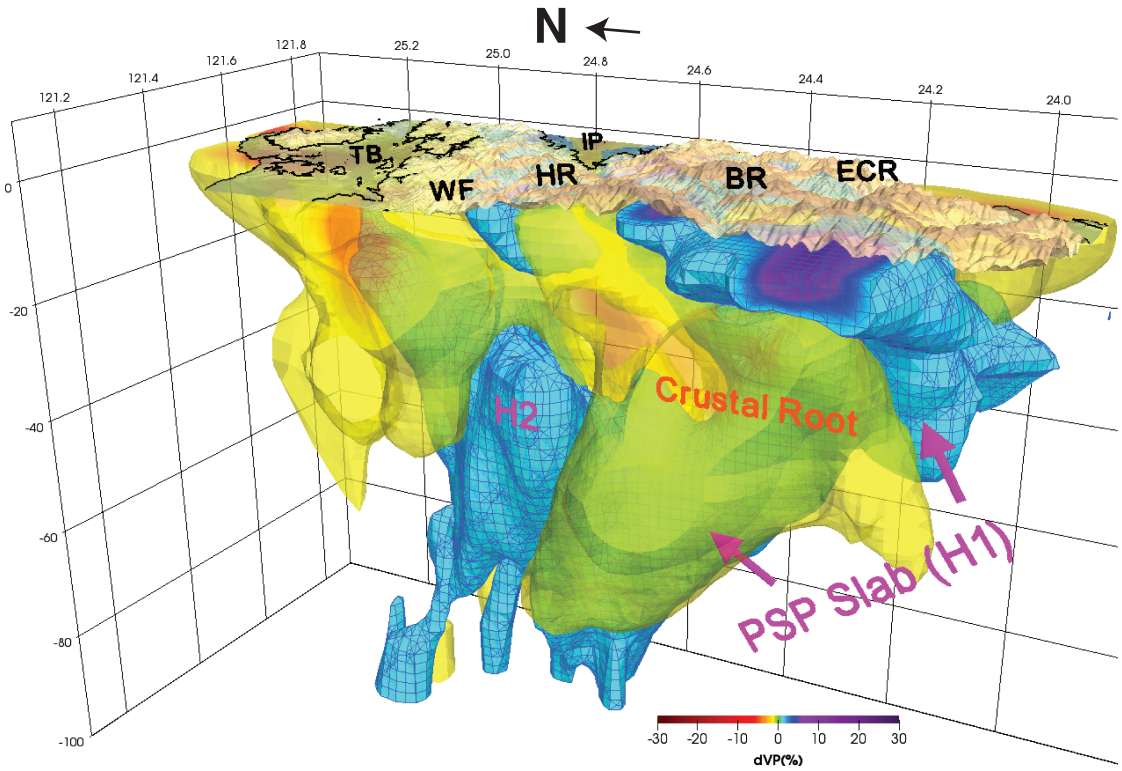

Figure 9. A 3-D visualization of the resulting velocity structures from SW to NE showing the contact areas of the two high V_p anomalies (H1 and H2) at depths greater than 40 km beneath NE Taiwan.

First, we examine the low V_p anomalies beneath the Taipei Basin and the Tatun Volcano Group (L2) that exhibit conspicuous features above 20 km. According to previous tomographic results (Huang et al., 2014; Kuo-Chen et al., 2012) on a broader scale to the south, the structures at shallow depths beneath the western Coastal Plain and Western Foothills tend to exhibit low V_p and low V_s anomalies, which are attributed to the continental crust, with additional contributions from deposited sediments (see Figure 5 of Huang et al. (2014)). In this respect, this area can be considered to be west of a deformation front due to the orogeny of the north Taiwan mountain belt a few million years ago. However, unlike the mountainous regions to the south, this area also hosts the Northern Taiwan Volcanic Zone (NTVZ). Based on the geochemical characteristics of its magmatism, the NTVZ likely resulted from an upwelling of the asthenosphere associated with the extensional collapse of the northern Taiwan mountain belt in the Pliocene-Pleistocene epoch with the subsequent involvement of subduction components (Wang et al., 2004). Therefore, mechanisms related to the NTVZ formation may alternatively contribute to this low V_p anomaly. As for the low V_p anomalies beneath the Ilan Plain (L1), they are surrounded by high V_p anomalous structures (H3), which correspond well to the metamorphic rocks in the northern Taiwan mountain belt and are similar to the patterns in central Taiwan. Both low V_p anomalies beneath the Ilan Plain and Kueishan Island can be traced to a deeper origin in the eastern offshore region (Figure 7). This justifies the conventional view that the Ilan Plain represents the SW end of the Okinawa Trough, which opened on a preexisting metamorphic mountain belt. Finally, low V_p anomalies below 20-km depth can be generally divided into two groups. The one located beneath the Central Range (Figure 9) has been interpreted as the thickened crustal root induced by the PSP–EUP collision (e.g., Huang et al., 2014; Kuo-Chen et al., 2012), and the other one, L3 in the mantle wedge (Figure 8), has been explained as serpentinization within the upper plate (Chou et al., 2009; Huang et al., 2014), a subduction channel with eroded forearc debris and sediments (Cloos & Shreve, 1988), or migration of fluids caused by slab dehydration (Cagnioncle et al., 2007; Lin et al., 2004).

In section 1, we mentioned four geophysical observations that can be used to distinguish model predictions between those of the tear and breakoff models. Among them, (a) the EUP-PSP junction in East Taiwan and

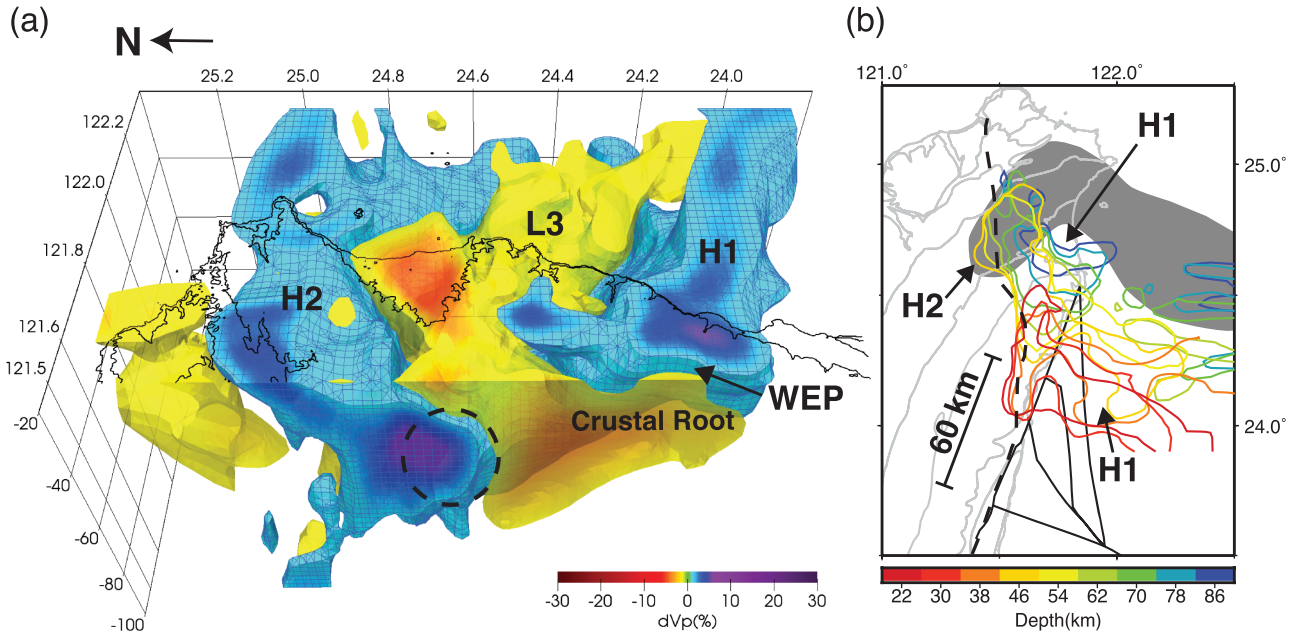

Figure 10. The upper mantle configuration of the EUP-PSP junction beneath NE Taiwan. (a) A 3-D visualization of the *P* wave velocity perturbations. The dashed circle indicates the contact between the two high V_p anomalies, H1 and H2, at a depth of approximately 45 km. WEP indicates the western edge of the subducted PSP slab. (b) Projected contours of the PSP slab (H1) at nine different depths. The 46-km depth contours suddenly extend northward due to the merging of the two high V_p anomalies. The gray area shows the outline of the high V_p region in the mantle wedge (H2) at a depth of 38 km. The dashed line illustrates the western edge of the PSP slab as determined by Wu et al. (2009). The solid lines indicate the surface boundaries between EUP and PSP specified by the four models of the EUP-PSP junction (Figure 1).

(b) the west edge of PSP (WEP) beneath North Taiwan are testable using results of tomographic studies. We further establish, from the geodynamical perspective, that the EUP-PSP boundary predicted by the breakoff and subducting indenter model should be the same, because the mantle window opened by the detached Eurasian lithosphere beneath North Taiwan would facilitate the westerly movement of the Philippine Sea slab and thus the subducting indenter in East Taiwan. The same pattern would in general predict that the EUP-PSP junction follows Model IV and that the WEP beneath North Taiwan can reach westerly as far as those under the Tatun Volcano Group, in contrast with those predicted by the tear model. Next, we determine the WEP and the EUP-PSP junction using high V_p anomalies of PSP (H1) deeper than 20 km (Figure 10a) to examine with those predicted by the subducting indenter model. To trace the 3-D variations of WEP, we draw contour lines of the junction (+1% V_p anomaly) at different depths between 22 and 86 km at 8-km intervals and color-keyed with depth (Figure 10b). The WEP thus derived is in general consistent with those (dashed line in Figure 10b) determined by Wu et al. (2009); however, at depths between 46 and 70 km, the contour lines shift to the west of the dashed line because H2 and H1 merge. On the other hand, to trace the top of PSP upward to the surface is out of the question as limited by the southern boundary of our velocity model (23.86°N). However, the fact that contour lines of the top of PSP between 22 and 54 km follow the trend of model IV on the EUP-PSP junction favors the proposal of Wu et al. (2009). According to Wu et al. (2009), we extend the model IV junction at the surface with a 20° dip to a depth of 22 km, resulting in about 60-km horizontal distance to the NE. The resulting location almost coincides with the 22-km depth contour of our study and validates the location of model IV (Figure 10b). Again, the high-resolution 3-D tomographic results agree with Wu et al. (2009) on model IV EUP-PSP junction in the extrapolation manner. In conclusion, features of high V_p anomalous PSP in this study comply with those predicted by the subducting indenter model and thus favor the breakoff model over the tear model.

The observations of a high V_p anomalous region in the depths between 20 and 80 km beneath NE Taiwan and offshore (H2) are robust not only in this study but also in previous ones (e.g., Huang et al., 2014). According to Leech (2001), eclogitization of rocks may explain the greater than 8-km/s *P* wave velocities at the depth range. Fluids play a key role in kinetics of eclogitization, and the two typical locations of

eclogitization in a collisional orogen are (i) the subducting crust and (ii) the base of the crustal root of the overriding crust. Eclogitization of the downgoing slab crust can provide an additional negative buoyancy force that helps to drive slab detachment (Huangfu et al., 2016), and an example of seismic imaging of such a slab can be seen in the Lesser Antilles (Paulatto et al., 2017). The lesser amount water contained by eclogite-facies metabasalts (0.8–0.0 wt %) may explain the observations of high-Q *P* waves of H2 (Ko et al., 2012). Putting together the characteristics of eclogitization for explanations of H2, while fluids could be provided by dehydration reactions of subducted PSP slab (H1), the two typical locations of eclogitization make both models plausible—(i) for the breakoff model and (ii) for the tear model. If H2 represents eclogitization of the subducting crust of the breakoff model, it corresponds to the region where the previous subducted EUP plate was detached (Teng et al., 2000) and H2 would be remains of the upper part slab after detachment. Accordingly, we would expect remains of the detached lower part of slab existing deep in the mantle, which is beyond the scope of this study.

As a final remark, what was missing in both models is validation from the geodynamic aspects. How the NW propagation of PSP tore the EUP lithosphere is not addressed in the tear model, neither is how the EUP slab detached to facilitate the west movement of PSP in the breakoff model. Recently, detachment of subducting slab due to subduction/collision of continental lithosphere has been modeled numerically (Huangfu et al., 2016; Menant et al., 2016). Results suggest that the subduction/collision of the Eurasian lithosphere alone is enough to drive detachment of the subducted slab. However, there need to be more efforts to establish the relationships between the features in the simulations (e.g., the retreat of the oceanic trench, the extrusion and stretching of the overriding plate, and the slab upbending upon detachment) and the tectonic features in NE Taiwan (e.g., the extensional collapse of the northern Taiwan mountain belt, the formation of the NTVZ, and the opening of the Okinawa Trough).

6. Conclusions

We conducted a high-resolution *P* wave tomographic study of NE Taiwan using existing network data combined with a dense Texan array on the Ilan Plain. The additions of the dense array data mainly enhance the resolution of shallow structures, especially those beneath the Ilan Plain. While the general features are consistent with those of previous studies, the high-resolution results for the specific region were used to examine proposals on mechanisms of subduction polarity flipping in NE Taiwan. First, the breakoff and subducting indenter model share the same predictions geodynamically that the EUP-PSP junction follows Model IV and that the WEP beneath North Taiwan can reach westerly as far as those under the Tatun Volcano Group. The high V_p anomalous PSP imaged in this study features a slab extending northwestward to a depth of more than 100 km beneath the Taipei Basin, and the extrapolated EUP-PSP junction locates at 23.7°N east coast of Taiwan. Both comply with predictions of the subducting indenter model and thus favor the breakoff model over the tear model. Second, the anomalously high V_p anomalous area in the mantle wedge of the PSP slab could be eclogitization of the subducting crust or the base of the crustal root of the overriding crust. Third, the areas beneath the Taipei Basin and the Tatun Volcano Group exhibit conspicuously low V_p anomalies at depths extending to 20 km and appear to be connected to the low V_p anomalies in the mantle wedge, suggesting that the PSP slab was involved in the formation of the NTVZ. Lastly, the low V_p anomalies beneath the Ilan Plain appear to be confined to depths above 10 km and to originate from offshore low V_p anomalous structures; this confirms that they correspond to the southwestern end of the Okinawa Trough.

Acknowledgments
This work was supported by the Taiwan Earthquake Research Center (TEC) funded through National Science Council (NSC) of Taiwan with grants 104-3113-M-002-001, 105-2116-M-008-004, 105-3113-M-002-001, 106-2116-M-008-004, and 107-2116-M-008-010. The TEC contribution number for this article is 00154. Equipment was provided by TEC. Thanks to C.H. Chang (CWB, Taiwan) for providing the CWBSN data, W.T. Liang (IES, Taiwan) for helping in data archiving, H. Kuo-Chen (NCU, Taiwan) for consulting on the usage of FDtomo, and Craig R. Bina (NU, USA) for the help with editing the manuscript. We thank two anonymous reviewers for the constructive opinions. The arrival-time data from the dense Texan array on the Ilan Plain are available from https://zenodo.org (Su et al., 2019). Data from the permanent stations are archived in the Geophysical Database Management System (http://gdms.cwb.gov.tw/index.php). Several figures were prepared with the Generic Mapping Tool (Wessel & Smith, 1998) and ParaView (Ayachit, 2015).

References

Allen, R. (1982). Automatic phase pickers: their present use and future prospects. *Bulletin of the Seismological Society of America*, *72*(6B), S225–S242.

Angelier, J., Bergerat, F., Chu, H. T., & Lee, T. Q. (1990). Tectonic analyses and the evolution of a curved collision belt: The Hsiiehshan Range, northern Taiwan. *Tectonophysics*, *183*, 77–96. https://doi.org/10.1016/0040-1951(90)90189-F

Ayachit, U. (2015). *The ParaView guide: A parallel visualization application*. Clifton Park, NY: Kitware. ISBN 978–1930934306

Bijwaard, H., Spakman, W., & Engdahl, E. R. (1998). Closing the gap between regional and global travel time tomography. *Journal of Geophysical Research*, *103*(B12), 30055–30078. https://doi.org/10.1029/98JB02467

Cagnioncle, A. M., Parmentier, E. M., & Elkins-Tanton, L. T. (2007). Effect of solid flow above a subducting slab on water distribution and melting at convergent plate boundaries. *Journal of Geophysical Research*, *112*, B09402. https://doi.org/10.1029/2007JB004934

Chen, K. X., Chen, P. F., Chen, L. W., Yao, H., Fang, H., & Su, P. L. (2016). South Ilan Plain High-Resolution 3-D S-Wave Velocity from Ambient Noise Tomography. *Terrestrial, Atmospheric and Oceanic Sciences*, *27*(3), 375–385. https://doi.org/10.3319/TAO.2016.01.29.02(TEM

Chen, Y. L. (1995). Three dimensional velocity structure and kinematic analysis in Taiwan area (master's thesis). Zhongli District, Taoyuan City, Taiwan: National Central University. (in Chinese with English abstract)

Chou, H. C., Kuo, B. Y., Chiao, L. Y., Zhao, D., & Hung, S. H. (2009). Tomography of the westernmost Ryukyu subduction zone and the serpentinization of the fore-arc mantle. *Journal of Geophysical Research*, *114*, B12301. https://doi.org/10.1029/2008JB006192

Cloos, M., & Shreve, R. L. (1988). Subduction-channel model of prism accretion, melange formation, sediment subduction, and subduction erosion at convergent plate margins: 1. Background and description. *Pure and Applied Geophysics*, *128*(3–4), 455–500. https://doi.org/10.1007/BF00874548

Engdahl, E. R., van der Hilst, R., & Buland, R. (1998). Global teleseismic earthquake relocation with improved travel times and procedures for depth determination. *Bulletin of the Seismological Society of America*, *88*(3), 722–743.

Font, Y., Liu, C. S., Schnurle, P., & Lallemand, S. (2001). Constraints on backstop geometry of the southwest Ryukyu subduction based on reflection seismic data. *Tectonophysics*, *333*, 135–158. https://doi.org/10.1016/S0040-1951(00)00272-9

Ho, C. S. (1986). A synthesis of the geologic evolution of Taiwan. *Tectonophysics*, *125*(1–3), 1–16. https://doi.org/10.1016/0040-1951(86)90004-1

Hou, C. S., Hu, J. C., Ching, K. E., Chen, Y. G., Chen, C. L., Cheng, L. W., et al. (2009). The crustal deformation of the Ilan Plain acted as a westernmost extension of the Okinawa Trough. *Tectonophysics*, *466*(3-4), 344–355. https://doi.org/10.1016/j.tecto.2007.11.022

Hsu, S. K., Liu, C. S., Shyu, C. T., Liu, S. Y., Sibuet, J. C., Lallemand, S., et al. (1998). New gravity and magnetic anomaly maps in the Taiwan-Luzon region and their preliminary interpretation. *Terrestrial, Atmospheric and Oceanic Sciences*, *9*(3), 509–532.

Hsu, Y. J., Yu, S. B., Simons, M., Kuo, L. C., & Chen, H. Y. (2009). Interseismic crustal deformation in the Taiwan plate boundary zone revealed by GPS observations, seismicity, and earthquake focal mechanisms. *Tectonophysics*, *479*(1), 4–18. https://doi.org/10.1016/j.tecto.2008.11.016

Huang, H. H., Wu, Y. M., Song, X., Chang, C. H., Lee, S. J., Chang, T. M., & Hsieh, H. H. (2014). Joint V_p and V_s tomography of Taiwan: Implications for subduction-collision orogeny. *Earth and Planetary Science Letters*, *392*, 177–191. https://doi.org/10.1016/j.epsl.2014.02.026

Huangfu, P., Wang, Y., Li, Z., Fan, W., & Zhang, Y. (2016). Effects of crustal eclogitization on plate subduction/collision: implication for India-Asia collision. *Journal of Earth Science*, *27*(5), 727–739. https://doi.org/10.1007/s12583-016-0701-9

Kanamori, H., Lee, W. H., & Ma, K. F. (2012). The 1909 Taipei earthquake—implication for seismic hazard in Taipei. *Geophysical Journal International*, *191*(1), 126–146. https://doi.org/10.1111/j.1365-246X.2012.05589.x

Kao, H., Shen, S. J., & Ma, K. F. (1998). Transition from oblique subduction to collision: Earthquakes in the southernmost Ryukyu arc-Taiwan region. *Journal of Geophysical Research*, *103*(B4), 7211–7229. https://doi.org/10.1029/97JB03510

Ko, Y. T., Kuo, B. Y., Wang, K. L., Lin, S. C., & Hung, S. H. (2012). The southwestern edge of the Ryukyu subduction zone: a high Q mantle wedge. *Earth and Planetary Science Letters*, *335–336*, 145–153. https://doi.org/10.1016/j.epsl.2012.04.041

Kuo-Chen, H., Wu, F. T., & Roecker, S. W. (2012). Three-dimensional P velocity structures of the lithosphere beneath Taiwan from the analysis of TAIGER and related seismic data sets. *Journal of Geophysical Research*, *117*, B06306. https://doi.org/10.1029/2011JB009108

Lallemand, S., Font, Y., Bijwaard, H., & Kao, H. (2001). New insights on 3-D plates interaction near Taiwan from tomography and tectonic implications. *Tectonophysics*, *335*(3), 229–253. https://doi.org/10.1016/S0040-1951(01)00071-3

Lallemand, S. E., Liu, C. S., & Font, Y. (1997). A tear fault boundary between the Taiwan orogen and the Ryukyu subduction zone. *Tectonophysics*, *274*, 171–190. https://doi.org/10.1016/S0040-1951(96)00303-4

Leech, M. L. (2001). Arrested orogenic development: Eclogitization, delamination, and tectonic collapse. *Earth and Planetary Science Letters*, *185*, 149–159. https://doi.org/10.1016/S0012-821X(00)0374-5

Lin, J. Y., Hsu, S. K., & Sibuet, J. C. (2004). Melting features along the western Ryukyu slab edge (northeast Taiwan): tomographic evidence. *Journal of Geophysical Research*, *109*, B12402. https://doi.org/10.1029/2004JB003260

Menant, A., Sternai, P., Jolivet, L., Guillou-Frottier, L., & Gerya, T. (2016). 3D numerical modeling of mantle flow, crustal dynamics and magma genesis associated with slab roll-back and tearing: The eastern Mediterranean case. *Earth and Planetary Science Letters*, *442*, 93–107. https://doi.org/10.1016/j.epsl.2016.03.002

Paulatto, M., Laigle, M., Galve, A., Charvis, P., Sapin, M., Bayrakci, G., et al. (2017). Dehydration of subducting slow-spread oceanic lithosphere in the Lesser Antilles. *Nature Communications*, *8*, 15980. https://doi.org/10.1038/ncmms15980

Roecker, S., Thurber, C., Roberts, K., & Powell, L. (2006). Refining the image of the San Andreas Fault near Parkfield, California using a finite difference travel time computation technique. *Tectonophysics*, *426*(1), 189–205. https://doi.org/10.1016/j.tecto.2006.02.026

Shin, T. C., Chang, C. H., Pu, H. C., Lin, H. W., & Leu, P. L. (2013). The Geophysical Database Management System in Taiwan. *Terrestrial, Atmospheric and Oceanic Sciences*, *24*, 11–18. https://doi.org/10.3319/TAO.2012.09.20.01(T

Sibuet, J. C., Letouzey, J., Barbier, F., Charvet, J., Foucher, J. P., Hilde, T. W., et al. (1987). Back arc extension in the Okinawa Trough. *Journal of Geophysical Research*, *92*(B13), 14041–14063. https://doi.org/10.1029/JB092iB13p14041

Su, P. L., Chen, P. F., & Wang, C. Y. (2019). *P*-wave arrival data of Ilan Texan Array (Version 1.0) [Dataset]. Zenodo. https://doi.org/10.5281/zenodo.3406096

Suppe, J. (1984). Kinematics of arc-continent collision, flipping of subduction, and backarc spreading near Taiwan. *Memoir of Geological Society of China*, *6*, 21–33.

Teng, L. S., Lee, C. T., Tsai, Y. B., & Hsiao, L. Y. (2000). Slab breakoff as a mechanism for flipping of subduction polarity in Taiwan. *Geology*, *28*(2), 155–158. https://doi.org/10.1130/0091-7613(2000)28<155:SBAAMF>2.0.CO;2

Wang, K. L., Chung, S. L., O'reilly, S. Y., Sun, S. S., Shinjo, R., & Chen, C. H. (2004). Geochemical constraints for the genesis of post-collisional magmatism and the geodynamic evolution of the northern Taiwan region. *Journal of Petrology*, *45*(5), 975–1011. https://doi.org/10.1093/petrology/egh001

Wessel, P., & Smith, W. H. (1998). New, improved version of Generic Mapping Tools released. *Eos, Transactions American Geophysical Union*, *79*(47), 579–579. https://doi.org/10.1029/98EO00426

Wu, F. T., Liang, W. T., Lee, J. C., Benz, H., & Villasenor, A. (2009). A model for the termination of the Ryukyu subduction zone against Taiwan: A junction of collision, subduction/separation, and subduction boundaries. *Journal of Geophysical Research*, *114*, B07404. https://doi.org/10.1029/2008JB005950

Wu, F. T., Rau, R. J., & Salzberg, D. (1997). Taiwan orogeny: thin-skinned or lithospheric collision. *Tectonophysics*, *274*, 191–220. https://doi.org/10.1016/S0040-1951(96)00304-6

Zhang, H., Thurber, C., & Rowe, C. (2003). Automatic *P*-wave arrival detection and picking with multiscale wavelet analysis for single-component recordings. *Bulletin of the Seismological Society of America*, *93*(5), 1904–1912. https://doi.org/10.1785/0120020241

Zhao, D., Wang, Z., Umino, N., & Hasegawa, A. (2009). Mapping the mantle wedge and interplate thrust zone of the northeast Japan arc. *Tectonophysics*, *467*(1), 89–106. https://doi.org/10.1016/j.tecto.2008.12.017